PNAS RESEARCH ARTICLE | APPLIED PHYSICAL SCIENCES OPEN ACCESS

Concentration gradients in evaporating binary droplets probed by spatially resolved Raman and NMR spectroscopy

Alena K. Bell[a,1], Jonas Kind[b,1], Maximilian Hartmann[c], Benjamin Kresse[d], Mark V. Höfler[d], Benedikt B. Straub[e], Günter K. Auernhammer[e,f], Michael Vogel[d], Christina M. Thiele[b,2], and Robert W. Stark[a,2]

Edited by David Weitz, Harvard University, Cambridge, MA; received June 29, 2021; accepted February 27, 2022

Understanding the evaporation process of binary sessile droplets is essential for optimizing various technical processes, such as inkjet printing or heat transfer. Liquid mixtures whose evaporation and wetting properties may differ significantly from those of pure liquids are particularly interesting. Concentration gradients may occur in these binary droplets. The challenge is to measure concentration gradients without affecting the evaporation process. Here, spectroscopic methods with spatial resolution can discriminate between the components of a liquid mixture. We show that confocal Raman microscopy and spatially resolved NMR spectroscopy can be used as complementary methods to measure concentration gradients in evaporating 1-butanol/1-hexanol droplets on a hydrophobic surface. Deuterating one of the liquids allows analysis of the local composition through the comparison of the intensities of the C–H and C–D stretching bands in Raman spectra. Thus, a concentration gradient in the evaporating droplet was established. Spatially resolved NMR spectroscopy revealed the composition at different positions of a droplet evaporating in the NMR tube, an environment in which air exchange is less pronounced. While not being perfectly comparable, both methods—confocal Raman and spatially resolved NMR experiments—show the presence of a vertical concentration gradient as 1-butanol/1-hexanol droplets evaporate.

Raman | NMR | sessile droplet | evaporation | concentration gradient

Significance

Imagine you spill your drink and miss some spots when cleaning up. The next morning you notice that the stains look quite different on different surfaces. What has happened? In droplets of liquid mixtures, the components evaporate at different rates, which leads to gradients in concentration and surface tension. These gradients can cause, for example, so-called Marangoni flows, which in turn affect the evaporation process. To better understand evaporation-induced liquid flows, the concentration gradients have to be measured without disturbing the liquid. Marker molecules might be surface-active or even may affect the evaporation process. We report here on marker-free and contactless measurements of concentrations by spatially resolved Raman and NMR spectroscopy in evaporating binary droplets.

Evaporating droplets occur in various contexts such as inkjet printing (1, 2), heat transfer, or daily phenomena such as drying coffee stains (3, 4). In many applications, such as painting (5), cleaning, gluing, or printing (6), where liquid mixtures are used, the evaporation of a droplet is a complex process because the concentration profile within the droplet varies over time. To improve the controllability and predictability of the technical processes, it is essential to characterize the transport phenomena during the drying process. The measurement of the droplet composition is a crucial element and has to be carried out with sufficient spatial and temporal resolution. In particular, spectroscopic methods are promising tools for contactless concentration measurements of liquid mixtures.

The evaporation of a droplet is governed by physical properties such as surface tension (7), density (8–10), vapor pressure (11), and boiling temperature. Additionally, concentration gradients can evolve in liquid mixtures (12). These gradients are driven by thermal gradients due to the enthalpy of evaporation (droplet cooling) or on heated surfaces, by surface tension gradients induced by preferential evaporation of one component or by density gradients for droplets composed of liquids with different densities like water and glycerol (13). The evaporation rates of the components can vary over the droplet surface. For sessile droplets with contact angles smaller than 90°, for example, the evaporation rates are higher at the three-phase contact line (14). These thermal or surface tension gradients can induce flow inside the droplet called Marangoni flow. This flow leads to concentration gradients across the droplet (7–10). The direction of the gradient depends on the density and surface tension. A direct application of this principle is, for instance, Marangoni cleaning in semiconductor technology (15).

The investigation of the composition of sessile drops on the microliter scale, as they occur in inkjet printing or other technical processes, poses a challenge because the typical length scales of interest are smaller than the capillary length. In bulk samples, the composition can be examined in a straightforward manner with chromatographic methods such as gas chromatography and high-performance liquid chromatography or spectroscopic methods such as NMR spectroscopy, infrared spectroscopy, and Raman spectroscopy. However, for the investigation of sessile droplets, a high spatial and temporal resolution is required. For this purpose, confocal Raman spectroscopy and spatially resolved NMR spectroscopy are powerful tools. For both techniques, concentration determination is straightforward if at least two signals of the components of interest are baseline-separated. NMR is intrinsically calibration-free, whereas Raman

Author contributions: G.K.A., M.V., C.M.T., and R.W.S. designed research; A.K.B., J.K., M.H., B.K., M.V.H., and B.B.S. performed research; A.K.B., J.K., M.H., B.K., M.V.H., and B.B.S. contributed new reagents/analytic tools; A.K.B., J.K., M.H., B.K., M.V.H., and B.B.S. analyzed data; and A.K.B., J.K., M.H., B.K., M.V.H., B.B.S., G.K.A., M.V., C.M.T., and R.W.S. wrote the paper.

The authors declare no competing interest.

This article is a PNAS Direct Submission.

[1]A.K.B. and J.K. contributed equally to this work.

[2]To whom correspondence may be addressed. Email: cthiele@thielelab.de or robert.stark@tu-darmstadt.de.

This article contains supporting information online at http://www.pnas.org/lookup/suppl/doi:10.1073/pnas.2111989119/-/DCSupplemental.

Published April 4, 2022.

spectroscopy requires calibration through reference experiments (16–18). Both approaches allow the quantification of concentration gradients in sessile droplets, as is shown here.

In Raman microscopy, good spatial resolution can be achieved in a confocal setup. The components of mixtures can be distinguished via specific vibrations for different functional groups or through a careful analysis of the Raman signals in the fingerprint region (<1,500 cm^{-1}). For example, binary mixtures of ethanol and water can be characterized in a straightforward manner (17). If, however, both liquids have a similar chemical structure, the discrimination of the components might be hampered by signal overlap in the C–H stretching region (2,800 to 3,000 cm^{-1}); e.g., in such cases, Raman signals in the fingerprint region (<1,500 cm^{-1}) might be used for the identification of the species. However, these signals often provide a poor signal-to-noise ratio, which makes large integration times necessary. Thus, the image rate or resolution is so low that even slow diffusion processes are hardly resolved. Here, Raman stable isotope probing (SIP), which has been developed to monitor metabolic processes in microbiology, offers a solution (19). The basic idea of Raman SIP is to replace the proton in the C–H with deuterium in one of the mixture components such that the C–D stretching region occurs at roughly $1/\sqrt{2}$ times the C–H stretching and falls into a region with very weak or even without signals from the protonated liquid component. Thus, the concentration in a binary mixture can be calculated in a straightforward manner from the ratio of the integrated Raman intensities I_{CD}/I_{CH} of the respective stretching vibrations.

Compared to Raman microscopy, where localization is achieved by scanning the focal point across the region of interest, in NMR experiments localization is achieved by using magnetic field gradients. Usually, one avoids phase boundaries (especially liquid–gas interfaces) in NMR experiments because they disturb the magnetic field homogeneity and reduce the spectral quality in terms of line shape and baseline separation of the resonances. Nevertheless, it has been shown that MRI can be used to characterize freezing water droplets (20), the infiltration of water into asphalts (21), and the evaporation of sessile droplets from porous surfaces (22–24). Additionally, NMR can be used to quantify the composition of binary droplets during evaporation (25).

Thus, the use of both complementary approaches to characterize evaporating binary droplets may be beneficial. In this article, we discuss the capabilities of Raman SIP and NMR techniques to analyze the evolution of the composition of an evaporating sessile binary droplet. As a model system, a binary mixture of 1-butanol and 1-hexanol was used. This mixture shows a low volatility such that the evaporation process can be captured with both Raman and NMR spectroscopies. With Raman spectroscopy, it was possible to observe concentration gradients of 1-butan-d_9-ol over the height of the droplet during evaporation. NMR techniques were examined in terms of the capability to observe the evaporation of 1-butanol and yield time-dependent droplet composition with spatially resolved ^{1}H-NMR spectra. Furthermore, the contours of the evaporating droplets were tracked by optical measurements to characterize the time-dependent changes in the droplet dimensions. Flows induced by the concentration gradients were confirmed by astigmatic particle tracking velocimetry.

Results

Binary Droplets. Five different systems were considered in this work: pure 1-butanol, pure 1-butan-d_9-ol (referred to as 1-butanol-d_9), pure 1-hexanol, and mixtures of 1-butanol/1-hexanol and 1-butanol-d_9/1-hexanol. The relevant parameters of the substances are given in *SI Appendix*, Table S1. The evaporation of binary droplets composed of 1-butanol/1-hexanol was investigated. Both alcohols have lower surface tensions than water, so a droplet of a 1-butanol/1-hexanol mixture has a smaller contact angle than a droplet of pure water. In the binary mixture, 1-butanol was expected to be the more volatile component because it has a lower boiling point and higher vapor pressure. As a result, a sessile binary droplet composed of 1-butanol and 1-hexanol with a contact angle below 90° shows an enhanced evaporation rate for 1-butanol at the three-phase contact line. Thus, flows in the droplet are driven by concentration gradients and gradients of the surface tension (Marangoni flow).

For Raman imaging, isotope-labeled fluids were used. The ^{2}H isotopologues (compounds were the hydrogen atoms are replaced by the heavy isotope deuterium) of both alcohols are commercially available, so lengthy deuteration procedures were not needed, and 1-butanol-d_9 was used for Raman SIP. The peak of the C–D stretching vibration served as a marker. Due to the approximately doubled mass of the deuteron vs. the proton, the resonance frequency of the C–D vibration is decreased by a factor of roughly $\sqrt{2}$ compared to the C–H vibrations (26–33). It is expected that the evaporation behaviors of different isotopologues of an alcohol differ depending on the degree and position of deuteration, as density, hydrogen bonding, and intermolecular dispersion interactions are affected. Hence, we used 1-butanol-d_9 instead of 1-butanol-d_{10} to retain comparable intermolecular hydrogen bonding interactions, as in 1-butanol-d_9 the hydrogen of the hydroxy group is not replaced by a deuterium. Due to the effect of deuteration (*SI Appendix*, Table S1) on the density and intermolecular dispersion interactions, 1-butanol-d_9 has a slightly lower vapor pressure than 1-butanol-d_{10}. Hence, 1-butanol-d_9 is expected to evaporate somewhat slower than 1-butanol-d_{10}. This difference is much smaller than the difference to 1-hexanol. We considered this difference in evaporation rates negligible.

Confocal Raman Stable Isotope Imaging. Raman measurements were taken as depth image scans in the *xz* plane and were repeated continuously to track the evolution of the concentration profile. The measurements were slightly off the droplet center to monitor the vertical concentration gradient over the drop height. At the drop center axis the concentration should be height-independent, while the interplay between component-dependent evaporation rates and Marangoni flows sustains a concentration gradient (7–10).

First, reference measurements were performed with pure substances and mixtures of protonated substances (*SI Appendix*, Fig. S3). From the reference experiments, the time scales of evaporation could be extracted for the single components and mixtures of substances. The concentration profiles, however, could not be measured with sufficient resolution because the most prominent Raman bands at 2,900 cm^{-1} overlapped.

By using 1-butanol-d_9 overlapping C–H stretching bands are avoided. The Raman spectra of pure 1-butanol-d_9 and 1-hexanol are given in Fig. 1*A*, as well as the Raman spectrum of the mixture of both substances. As described above the C–H stretching band of 1-hexanol (2,800 to 3,000 cm^{-1}) and the C–D stretching band of 1-butanol-d_9 (2,000 to 2,400 cm^{-1}) are baseline separated. Hence, the ratio of the integrated band intensities can be used as a measure for the concentration (29) by using a calibration curve (16–18).

The measurements show different evaporation behaviors for the two alcohols of different chain lengths. The 1-butanol and

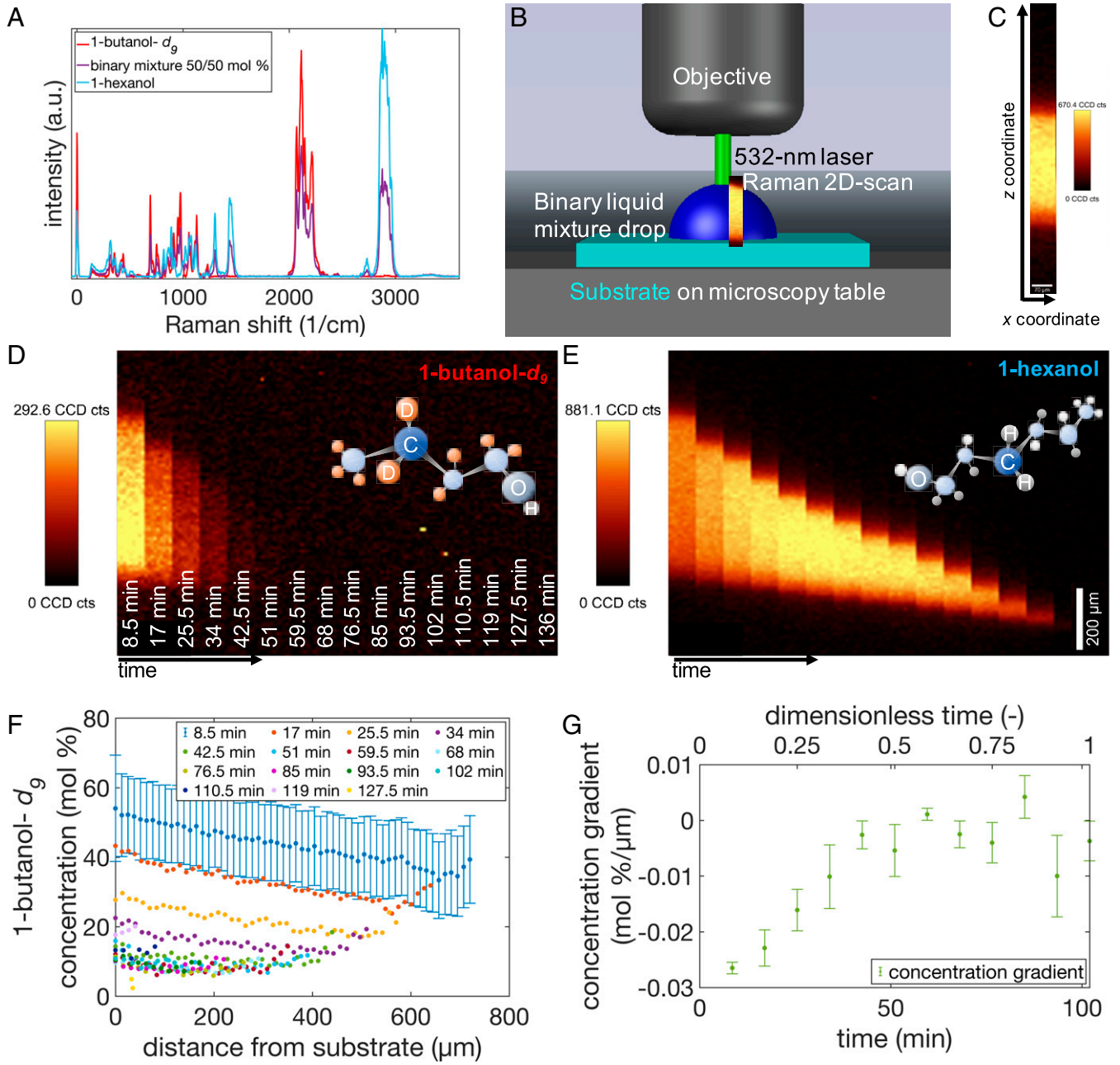

Fig. 1. (*A*) Raman spectra of 1-butanol-d_9 (red spectrum), 1-hexanol (blue spectrum), and a mixture of both substances in a ratio of 50:50 mol % (violet spectrum). The spectrum of the mixture shows a superposition of both pure components. The peaks used to calculate the concentration are 2,000 to 2,400 cm^{-1} (C–D, 1-butanol-d_9) and 2,800 to 3,000 cm^{-1} (C–H, 1-hexanol). (*B*) Sketch of the Raman experimental setup with microscope objective and table, substrate, laser, binary liquid mixture droplet and a Raman 3D scan. (*C*) Raman 2D depth scan with axes. In every pixel a spectrum (as in *A*) was taken and filtered. Many of these 2D scans taken after each other were combined in temporal sequences in *D* for the 1-butanol-d_9 and in *E* for the 1-hexanol signals. (*F*) Calculated concentration profiles for each scan. Error bars are shown for one measurement are representative and similar for the other data points. (*G*) The 1-butanol-d_9 concentration gradient over experimental data at a position slightly off-center of the droplet as sketched in *B*.

1-butanol-d_9 have lower boiling temperatures, higher vapor pressures, and higher surface tensions; they evaporated within 30 min. The 1-hexanol has a lower vapor pressure and thus evaporated much more slowly, in ∼190 min. The mixture of both substances had an intermediate evaporation time of almost 120 min.

Because the scans were taken through the liquid–gas interface, variations in the optical path had to be considered. One might think that refraction must be considered because the droplet acts as an additional lens in the optical path. A sketch to visualize the effect on a vertical line in a scan is given in *SI Appendix*, Fig. S4. Briefly, according to Snell's law, the transition from air ($n_{air} = 1$) to the curved surface of 1-butanol ($n_{but} = 1.3988$) or 1-hexanol ($n_{hex} = 1.418$) causes refraction of the laser focus in the direction of the drop center and changes the focal length of the system. This leads to a distortion of the image (the image is then compressed and slightly curved). In the center of the drop, i.e., close to the optical axis, compression or stretching prevails, while bending distortion can be neglected. For this reason, the measurements were conducted close to the center of the drop (optical axis) so that the scattering effects could be safely neglected. Raman spectra of the pure substances and the deuterated mixture, the experimental setup, and a single two-dimensional (2D) Raman scan are given in Fig. 1 *A*–*C*.

The intensity distribution of the peaks corresponding to the substances are given in the depth scans, shown in Fig. 1 *D* and *E*. The depth scans are raw data, i.e., they have not been corrected for the optical distortion. From left to right, the temporal sequence of scans of the same drop is shown. To calculate the concentration from these intensity distribution images, the calibration curve, given in *SI Appendix*, Fig. S3*E*, is needed. In Fig. 1*F* the concentration profile in every scan is displayed, and in Fig. 1*G* the concentration gradient over the experimental time is given.

From the confocal Raman scans in Fig. 1 *D* and *E*, the droplet height can be estimated from the interface between liquid and vapor (top of the stripes). Plotting the height of the 1-butanol-d_9/1-hexanol mixture droplet over time reveals that the height decreased in a nonlinear manner, which is explained by evaporation in stick-slip mode, which is a mixed mode of constant contact angle (CCA) and constant contact radius (CCR) modes. Initially, the height of the droplet decreased rapidly, and this process slowed. The initial fast decrease was correlated to the evaporation of the more volatile component (1-butanol or 1-butanol-d_9) of the 1-butanol/1-hexanol or 1-butanol-d_9/1-hexanol mixture. After most of the butanol component had evaporated, the 1-hexanol most likely evaporated as the pure substance. Additionally, a nonlinear, wave-like decrease in height was observed due to a stick-slip evaporation mode.

This observation agrees with contact angle goniometry data (*SI Appendix*). The concentration gradient for the 1-butanol-d_9/1-hexanol mixture can be calculated from the intensity distribution images in Fig. 1 *D* and *E*. The intensity distribution images (Fig. 1 *D* and *E*) show a faster 1-butanol-d_9 depletion in the upper part of the droplet than near the substrate. This distribution changed after the first four scans (34 min) when the more volatile 1-butanol-d_9 had evaporated such that only a 1-hexanol signal was detected. The highest 1-butanol-d_9 fraction (55 ± 15 mol %) was measured near the substrate in the first scan. At the liquid/gas interface, the 1-butanol-d_9 fraction was 40 ± 12.5 mol %. The vertical concentration profile is given in Fig. 1*F*, and the evolution of the concentration gradient is shown in Fig. 1*G*. In the first scans, a gradient of 0.024 ± 0.001 mol %/μm was observed, which decreased to nearly zero (0.003 ± 0.003 mol %/μm) after the first five scans. This was also observed in the intensity images and the concentration graph. The results also show that the 1-butanol-d_9 concentration decreased with time in the whole droplet. The lower detection limit of the 1-butanol-d_9 concentration was 12 ± 14 mol % due to the low signal-to-noise ratio. Additionally, the inspection of the Raman spectra after the first five or six scans indicated that 1-butanol-d_9 evaporated below the detection limit.

These concentration gradients in the bulk give rise to concentration (and probably temperature) gradients along the droplet surface. These surface gradients lead to surface tension gradients and induce Marangoni flows. To verify the Marangoni flows, astigmatism particle tracking velocimetry measurements were performed. From these measurements, a flow from the drop center along the drop surface toward the three-phase contact line and back to the bulk was observed, proving the existence of surface tension gradients. The details of these results are given in *SI Appendix* and the images in *SI Appendix*, Fig. S11.

Concentration Determination Using Spatially Resolved NMR Spectroscopy. The evaporation of 1-butanol/1-hexanol droplets was also observed using (non)spatially resolved NMR techniques as an independent and complementary characterization method. In contrast to Raman spectroscopy, it was not necessary to use deuterated 1-butanol. Both alcohols have similar chemical shifts for all resonances in isotropic bulk samples (Fig. 2). Further complications arose for small droplets on surfaces, as the magnetic field homogeneity is influenced by the large liquid–gas interface, so the resulting line width in NMR spectra did not allow for

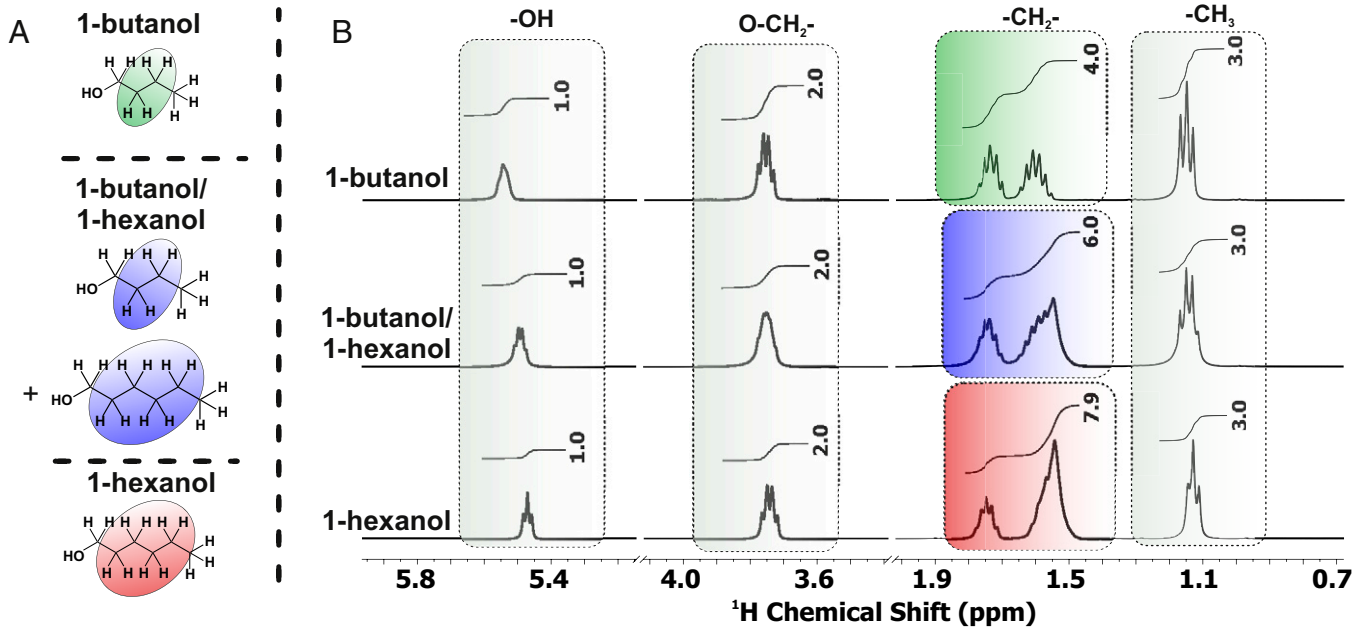

Fig. 2. (*A*) Chemical structures of 1-butanol and 1-hexanol. CH_2 resonances are highlighted. (*B*) ^{1}H NMR spectra (400 MHz, 300 K) of pure 1-butanol, a 50 mol % mixture of 1-butanol and 1-hexanol, and pure 1-hexanol measured as isotropic bulk samples in 5-mm NMR tubes. The NMR spectra were acquired with a single scan and 64,000 data points over a sweep width of 20 ppm within an acquisition time of 4.089 s. For all three spectra, the integrals of the hydroxy groups (-OH), methylene groups near the oxygen (O-CH_2), and methyl groups (-CH_3) show the same value (gray boxes). For pure 1-butanol, for the remaining methylene groups (-CH_2, green box), a signal integral of four is expected and obtained. For pure 1-hexanol, the remaining CH_2 groups have a signal integral of eight (red box). Hence, for a 50:50 mol % mixture of these two alcohols, a signal integral of six (blue box) is observed. This indicates the expected linear behavior with concentration.

direct analysis of the composition via integration of the resonances belonging to the two different species. Nevertheless, the molar ratios of 1-butanol and 1-hexanol in bulk samples and droplets could be determined from ^{1}H NMR spectra by comparing the integrals of CH_2 and CH_3 resonances. For pure 1-butanol, a ratio of 4:3 was expected, and for pure 1-hexanol, a ratio of 8:3 was expected (Fig. 2). For the 50 mol % mixture the ratio of the CH_2 and CH_3 resonances is 6:3. From this linear relation of integral ratio and composition a linear equation can be formulated. Here the fraction is given against the integral ratio giving a slope of 0.75 and an intercept of −1. Hence, the fraction can be calculated with Eq. **1** via using the measured integral ratio of CH_2 and CH_3 resonances:

$$X_{1-hexanol} = 0.75 \cdot \left(\frac{I_{CH_2}}{I_{CH_3}}\right) - 1$$
$$X_{1-butanol} = 1 - X_{1-hexanol}. \quad [1]$$

In contrast to bulk samples, for droplets artifacts due to differences in susceptibility are expected, which should be smaller at lower magnetic fields. Thus, molar fractions of 1-butanol and 1-hexanol in evaporating droplets of a 50:50 mol % mixture were examined with nonspatially resolved NMR spectroscopy at a low field (4.7 T). As a result, the time-dependent bulk composition of the droplet during evaporation was obtained (*SI Appendix*, Figs. S7 and S8). The concentration of the more volatile component $X_{butanol}$ decreased during evaporation but did not reach zero. Rather, it appeared to saturate at a concentration of slightly less than 20 mol %. Below this concentration experimental uncertainties did not allow further conclusions.

To minimize the effects of the liquid/gas interface on the line shape and width observed, PRESS (Point RESolved Spectra, in the following described as localized spectroscopy) (34, 35) NMR spectra were acquired within the droplet instead of measuring the whole droplet. Note that a different setup from the one above was applied (9.4 T). The voxel size and position were chosen in a way that no interphase was within the region of interest (Fig. 3).

To investigate whether it is possible to locally detect a concentration gradient during evaporation, three small voxels (0.2 mm × 0.2 mm × 0.2 mm) positioned above each other were selected so that spectra were obtained over the entire drop height of initially approximately 650 μm (see colored boxes in Fig. 3). In contrast to nonspatially resolved NMR spectra, in the PRESS spectra acquired with this voxel size, the overall linewidth was significantly smaller. As a result, the CH_2 and CH_3 resonances were baseline-separated (*SI Appendix*, Figs. S7 and S8). Hence, the molar fractions of 1-butanol and 1-hexanol could be calculated using Eq. **1**.

A faster decrease in butanol concentration was observed for the upper voxel than for the middle and lower voxels (Fig. 4). For the topmost voxel, the 1-butanol fraction decayed to zero within 500 min. In the bottom voxel, 1-butanol could be detected for up to 2,500 min. Hence, a vertical concentration gradient was present. At t = 0, a molar fraction of 40 mol % 1-butanol was observed in the top voxel, while in the bottom and middle voxel, a fraction of 50 mol % was observed, which is in agreement with the Raman data. Hence, the total concentration gradient of 1-butanol could be roughly estimated as 10 mol %. As the droplet height at t = 0 was ∼600 μm, the concentration gradient equaled 0.017 mol %/μm. Since the measurements were carried out in three voxels and therefore with low spatial resolution, the calculated concentration gradient should be classified as an estimate. Note that no measurements could be carried out during a transfer dead time between droplet deposition outside the NMR spectrometer, inserting the sample, preparing the spectrometer, and the start of the first measurements, which already show a gradient. Thus, the gradient was generated quickly (less than the dead time of several minutes). The present data show that although the NMR tube can be considered as nearly closed, equilibrium between the vapor phase and the liquid is not established. If equilibrium were to occur, complete evaporation of the droplet could not be observed, but this is the case.

At ∼500 min, at which time the 1-butanol fraction in the top voxel decayed to ∼0 to 5 mol %, a molar fraction of 20 mol % ± 5 mol % 1-butanol was observed in the bottom as well as in the middle voxel. Hence, the total concentration gradient of 1-butanol could be roughly estimated as 10 to 20 mol %. For an assumed droplet height of 500 μm, this equals a gradient of 0.02 to 0.04 mol %/μm. Within the shifted voxel the molar fraction of butanol is ∼12.5 to 15 mol %. Using this concentration, the total concentration gradient would be 5 to 8.5 mol %, yielding a gradient of 0.01 to 0.017 mol %/μm.

For both time points, the observed concentration gradients were of the same order of magnitude as those observed with Raman, albeit the evaporation rates were different due to the different measurement environments.

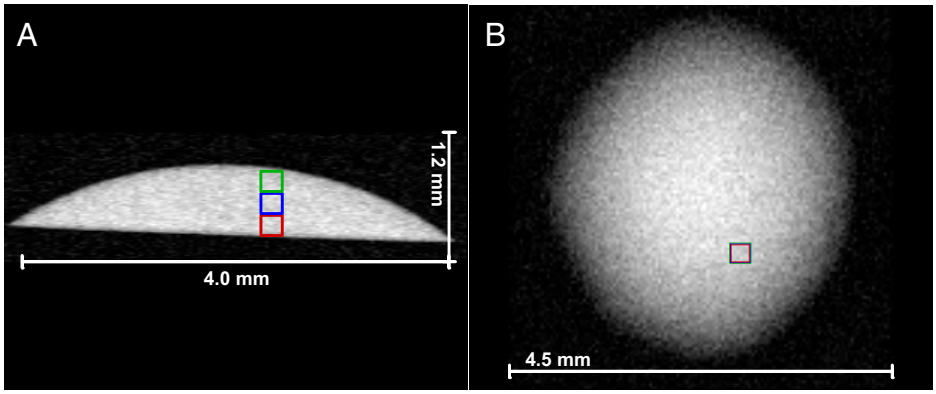

Fig. 3. (*A*) Sagittal RARE (40) VTR (Rapid Acquisition with Relaxation Enhancement with variable repetition time TR) image and (*B*) axial RARE (Rapid Acquisition with Relaxation Enhancement) image (40) of a fresh 1-butanol/1-hexanol droplet on a PFDTS surface. Both images are acquired at 400-MHz proton resonance frequency (9.4 T). The positions of the voxels used for PRESS are highlighted with colored boxes. Both images were acquired with a 128 × 128 matrix with a field of view of 4.5 × 4.5 mm and a slice thickness of 1 mm. For the sagittal image, a single scan with an echo time (TE) of 20 ms, a repetition time (TR) of 1,000 ms, and a RARE factor of 8 was used. For the axial image, two scans with TE = 20.83 ms and TR = 2,000 ms and a RARE factor of 8 were accumulated.

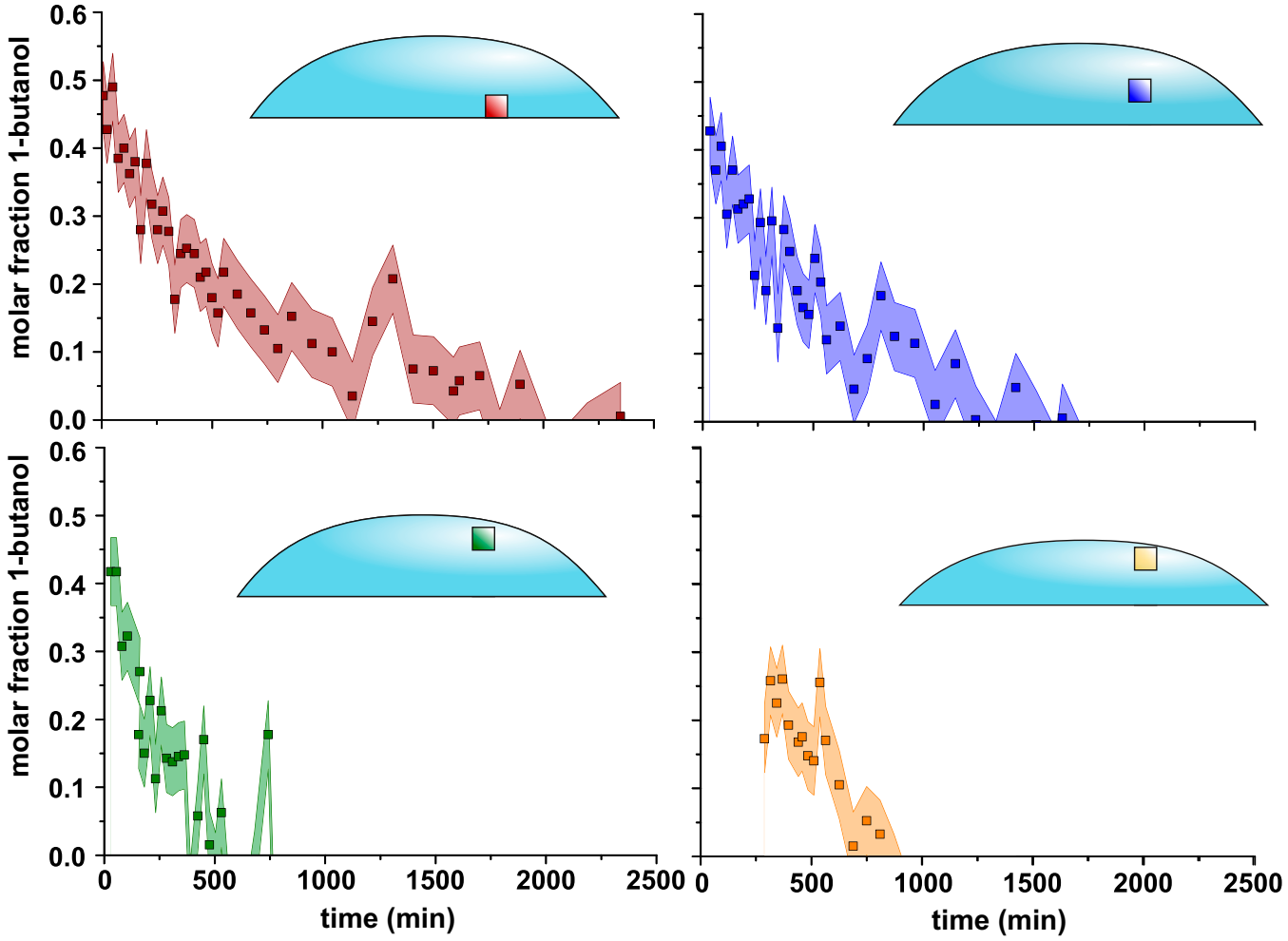

Fig. 4. Fraction of 1-butanol in four different voxels (0.2 × 0.2 × 0.2 mm) during evaporation over time t at 298.5 K. The voxel positions are indicated within the drawing. The PRESS NMR spectra were acquired with 64 scans, a repetition time of 4,000 ms and an echo time TE of 20 ms. For each free induction decay, 8,000 data points were acquired within an acquisition time of 998.4 ms. Bandwidth of the pulses was set to 5,400 Hz. The orange voxel is shifted downward compared to the green voxel to avoid a moving liquid/gas interphase within the voxel. The 1-butanol fraction is calculated by comparing the signal integrals of CH_2 and CH_3 resonances.

For the bottom voxel, the 1-butanol fraction rose at 1,250 min. We ascribe this observation to a change in the droplet shape at this point in time, which induced a change in the concentration field within the droplet.

During evaporation, the liquid–gas interface migrated from top to bottom so that the interface after a certain time was first in the upper voxel, later in the middle, and finally in the lowest voxel. This had two consequences. First, the amount of material in the voxel decreased as soon as the interface passed through the voxel. This caused the signal intensity, and thus the signal-to-noise ratio, to decrease. On the other hand, as described above, magnetic field inhomogeneities occurred at the interface, which had negative effects on the signal shape. Both a poor signal-to-noise ratio and wide line shapes can have a negative effect on the determination of the composition from the relative signal integrals. Therefore, as soon as the interface reached the top voxel, this voxel was shifted downward so that it overlapped with the middle voxel. From the moment the interface was in this shifted voxel, only the middle and bottom voxels were considered. The error (colored band in Fig. 4) was estimated from a PRESS spectrum of pure 1-hexanol (*SI Appendix*, Fig. S8). These errors of course propagated into the calculated concentration gradients, so the values given above are estimates.

Comparing the evaporation times of the same drops with the three methods, it is evident that the evaporation times were very different, although the same mixtures and the same liquid volumes were used for the droplets. The droplets that were investigated by Raman spectroscopy evaporated in the shortest time (~2 h), and those investigated with NMR spectroscopy took the longest time until full evaporation of the droplet time (~23 h). For the contact angle measurements, the droplets showed an intermediate evaporation time. This discrepancy was caused by the different surroundings and ambient conditions. The spatially resolved NMR spectroscopy measurements were taken in tubes, resembling a nearly closed system without any convective exchange of the gas phase, while the nonspatially resolved NMR spectroscopy measurements were taken with airflow through the probe head.

Within the NMR tube no active temperature or humidity regulation can be applied. Simple evaporation experiments with small water droplets (4.2 μL) show that the partial pressure (of water) within an NMR tube increases over a longer time (hours) until an atmosphere with high relative humidity (RH) is obtained due to the absence of convection. This time scale is longer than for 1-butanol as the vapor pressure of water is higher than the vapor pressure of 1-butanol. Hence, we assume that during evaporation of 1-butanol/1-hexanol droplets the

atmosphere within the NMR tube is saturated with 1-butanol and 1-hexanol slowing down the total evaporation rate of the droplet. For the Raman experiments it has to be assumed that convection of the atmosphere occurs and no saturation of the atmosphere with 1-butanol and 1-hexanol above the droplet occurs.

Furthermore, we assume that the temperature and humidity within the NMR spectrometer are comparable to the values of the NMR laboratory (~291 to 293 K, 35 to 45% RH). For contact angle goniometry, an ambient chamber with tunable humidity conditions was used. The droplets investigated by Raman spectroscopy were not surrounded by any chamber, and the humidity was not held constant in the laboratory, but typical temperatures are in the range of 291 to 293 K and RH is 40 to 60%. We assume that the absence or presence of convection of the surrounding has a larger impact on droplet evaporation rates than small deviation within temperature or humidity. Thus, a direct comparison of NMR and Raman results is difficult.

Discussion

With both complementary imaging spectroscopy methods, Raman SIP and spatially resolved NMR, the evolution of the concentration gradients in an evaporating binary droplet was characterized. The challenge of discriminating two chemically very similar components, here two alcohols, in vibration spectroscopy was solved by heavy isotope labeling (stable isotope probing). In contrast to previous methods, no additional markers, e.g., fluorophores, which may be surface-active themselves, are needed. Using ^{2}H isotopologues of one component influences evaporation properties to a neglectable extent, as long as strong intermolecular interactions such as hydrogen bonds are retained by using proper isotopologues such as 1-butanol-d_9. For the NMR experiments employed here, isotope labeling is not necessary; hence, this method can be considered a "marker-free" method. Raman SIP delivers concentration information with a high temporal and spatial resolution. Compared to Raman spectroscopy, NMR yields a lower spatial and temporal resolution, but the high atom specificity and very large variety of available NMR experiments, such as diffusion-ordered spectroscopy, MR imaging with different contrasts, relaxation measurements, and multidimensional experiments, make NMR a very promising method for examining drying processes, e.g., molecular diffusion changes during evaporation of droplets due to changes in viscosity. Additionally, with NMR, nontransparent liquids can be examined.

Overall, Raman and NMR can be considered a promising pair of complementary methods for the examination of evaporating droplets, as they are based on two different physical effects and show different spatiotemporal resolutions; both can be considered noninvasive and (nearly) marker-free. The concentration measurements carried out here were performed for a binary droplet of 1-butanol/1-hexanol on a hydrophobic PFDTS (1H,1H,2H,2H-perfluorodecyltrichlorosilane) surface. The contact angle measurements show evaporation behavior with a mixed mode between the CCA and CCR modes. Raman spectroscopy measurements indicate that evaporation rates are enhanced at the three-phase contact line. Both methods reveal that 1-butanol evaporates faster from the droplet, generating concentration gradients of up to 0.03 to 0.04 mol %/μm inside the sessile droplet. Both Raman and NMR measurements show that these gradients develop on a fast time scale, as for both methods a gradient is observed in the first measurement after droplet deposition. These concentration gradients give rise to a surface tension gradient at the surface of the droplet, which induces Marangoni flow, which is confirmed by astigmatic particle tracking velocimetry. The evolution of the concentration gradient can be obtained by Raman SIP imaging. Nevertheless, we note that the experimental conditions were different to some extent. The Raman experiments were done in laboratory conditions, without additional housing around the droplet, which makes the Raman setup an open system. Compared to that, the NMR experiment were performed on the bottom of a long tube (10 cm), which makes the conditions comparable to a nearly closed system.

Our approach to measuring concentration profiles with both methods opens the door to characterizing the evaporation process of miscible binary mixtures with different densities, surface tensions, vapor pressures, and boiling points. Thus, Raman SIP imaging and spatially resolved NMR are powerful tools for investigating mass transport processes in binary liquid mixtures not only in droplets but also in further applications where concentration profiles need to be characterized in microfluidics devices or polymer systems.

Materials and Methods

Materials. The 1-hexanol (CAS: 111-27-3, reagent grade; Sigma-Aldrich), 1-butanol (CAS: 71-36-3, 99%; Alfa Aesar), and 1-butan-d_9-ol (CAS: 25493-17-8, 99% grade; Sigma-Aldrich) were used as received.

For all measurement techniques, the substances were mixed at 50:50 mol %. The droplet volume for all measurements was set to 4.2 μL, and the droplets were placed on the substrates using 10-μL Hamilton syringes (Hamilton Company) or an Eppendorf pipette with 20-μL tips.

Silanized glass slides were used as substrates. For that purpose, PFDTS (CAS: 78560-44-8; abcr GmbH) was coated onto glass in a low-pressure chemical vapor deposition process that was designed to match the conditions of ref. 36 The protocol of all steps needed for silanization can be found in the supporting information of ref. 37.

Methods.

Raman spectroscopy. A confocal Raman microscope (alpha 300R; Witec GmbH) with a green laser (532 nm, Nd:YAG) at 1-mW laser power and a Nikon 10×/0.25 objective was used for the Raman spectroscopic concentration measurements. For the concentration measurements, depth image scans were performed with a size of 90 × 1,000 μm^2 (*xz* plane) in an upward direction. The integration time was 0.3 s per pixel with 9 × 100 pixels in each scan. These scans were repeated continuously every 8.5 min. A sketch of the experimental setup for the Raman experiments is given in Fig. 1*B*. The experiments were performed in the laboratory surrounding without a housing to control and maintain the surrounding conditions.

The background was subtracted, and cosmic rays were removed from the spectra by the software WITec Project 5 (WITec GmbH) before cross-sections were taken in the *z* direction to evaluate the concentration profiles. To calculate the concentration, the peak ratio between the Raman bands at 2,900 cm^{-1} (protonated substance) and 2,150 cm^{-1} (deuterated substance) was used, which was then correlated to the calibration curve of the respective mixture. These calibration curves were measured with point scans in the mixture with integration times of 3 × 5 s at 5-mW laser power for every defined mixture. All depth measurements within the binary mixture droplets were performed beside the center of the drop to find a possible concentration gradient. In the center of the droplet, the concentration should remain constant over the height (7, 8). The Raman experiments were performed under laboratory conditions (22.0 to 23.0 °C and 40 to 60% RH). Due to the lens effect of the droplet, the droplet height was recalculated as explained in *SI Appendix*, Fig. S4 *A–C*.

NMR spectroscopy. NMR spectra (Fig. 2 and *SI Appendix*, Fig. S7) and MR images (Fig. 3) were acquired with a Bruker Avance III HD spectrometer (400-MHz proton resonance frequency, 9.4 T) equipped with a narrow-bore micro 5 probe with x, y, z gradients and three GREAT 60 (A) gradient amplifiers

(25). All images and NMR spectra were acquired using an insert with a 10-mm coil tuned to the resonance frequency of ^{1}H at room temperature and without spinning of the sample. MRI and NMR data were acquired and processed using Paravision 6 and Topspin 3.1PV, respectively. For all experiments, standard sequences for FLASH (38, 39), RARE (40), and PRESS (34, 35) from the Bruker pulse sequence library were used. The acquisition parameters for the MR images and NMR spectra are given in the figure legends.

Humidity in the NMR tube is measured with a Honeywell humidity sensor.

All samples were prepared in 10-mm NMR tubes (Wilmad Labglas HT WG-4000) (22). Acrylate inserts were 3D-printed on a Pico2^{HD} 27 (Asiga) stereolithographic 3D printer using PlasCLEAR (Asiga) or Clear Resin BV-007 (MIICRAFT) photoresin. Hydrophobic surfaces were prepared as described above. These 7-mm round microscopy glasses (Plano) were glued to the 3D-printed inserts with cyanoacrylate superglue (Pattex; Henkel). Since the NMR tubes were nearly closed during the measurements, the NMR experiments were taken in a closed system which makes a comparison between the NMR and Raman experiments very difficult.

Additionally, NMR spectra of the entire droplet (*SI Appendix*, Fig. S5) were recorded in a 200-MHz (4.7-T) magnet using a custom-built probe and applying a Hahn Echo pulse sequence. With the use of a weaker magnetic field, it is assumed that magnetic field distortions due to different magnetic susceptibilities of the substrate, liquid, and air have a smaller impact on the resulting spectra. The in-house-built probe had a sample holder for a substrate and a solenoid radiofrequency coil similar to that presented in previous work (24). Droplets with sizes up to a couple of microliters could be investigated, and a continuous airflow of ∼5 L/min was applied.

Data Availability. Raw data have been deposited in TUdatalib (https://doi.org/10.48328/tudatalib-824.2) (41).

ACKNOWLEDGMENTS. This study was funded by the Deutsche Forschungsgemeinschaft Project ID 265191195 – SFB 1194, "Interaction between Transport and Wetting Processes" and Projects A02, A06, A07, and A08. We thank T. Gambaryan-Roisman and M. Heinz (Project A04 within CRC 1194) for sharing their Droplet EvolutioN: Impact, Imbibition, Spreading and Evaporation (DENISE) MATLAB algorithm.

Author affiliations: [a]Physics of Surfaces, Institute of Materials Science, Technical University of Darmstadt, 64287 Darmstadt, Germany; [b]Clemens-Schöpf-Institute for Organic Chemistry and Biochemistry, Technical University of Darmstadt, 64287 Darmstadt, Germany; [c]Institute for Nano- and Microfluidics, Technical University of Darmstadt, 64287 Darmstadt, Germany; [d]Institute of Condensed Matter Physics, Technical University of Darmstadt, 64289 Darmstadt, Germany; [e]Max Planck Institute for Polymer Research, 55128 Mainz, Germany; and [f]Abteilung Polymergrenzflächen, Leibniz-Institut für Polymerforschung Dresden e.V., 01069 Dresden, Germany

1. E. L. Talbot, L. Yang, A. Berson, C. D. Bain, Control of the particle distribution in inkjet printing through an evaporation-driven sol-gel transition. *ACS Appl. Mater. Interfaces* **6**, 9572–9583 (2014).
2. H. Wijshoff, Drop dynamics in the inkjet printing process. *Curr. Opin. Colloid Interface Sci.* **36**, 20–27 (2018).
3. D. Mampallil, H. B. Eral, A review on suppression and utilization of the coffee-ring effect. *Adv. Colloid Interface Sci.* **252**, 38–54 (2018).
4. A. Nilghaz, L. Zhang, W. Shen, Coffee stains on paper. *Chem. Eng. Sci.* **129**, 34–41 (2015).
5. S. Manukyan *et al.*, Imaging internal flows in a drying sessile polymer dispersion drop using Spectral Radar Optical Coherence Tomography (SR-OCT). *J. Colloid Interface Sci.* **395**, 287–293 (2013).
6. J. Z. Wang, Z. H. Zheng, H. W. Li, W. T. S. Huck, H. Sirringhaus, Dewetting of conducting polymer inkjet droplets on patterned surfaces. *Nat. Mater.* **3**, 171–176 (2004).
7. S. Karpitschka, F. Liebig, H. Riegler, Marangoni contraction of evaporating sessile droplets of binary mixtures. *Langmuir* **33**, 4682–4687 (2017).
8. C. Diddens, J. G. M. Kuerten, C. W. M. van der Geld, H. M. A. Wijshoff, Modeling the evaporation of sessile multi-component droplets. *J. Colloid Interface Sci.* **487**, 426–436 (2017).
9. C. Diddens *et al.*, Evaporating pure, binary and ternary droplets: Thermal effects and axial symmetry breaking. *J. Fluid Mech.* **823**, 470–497 (2017).
10. C. Diddens, Detailed finite element method modeling of evaporating multi-component droplets. *J. Comput. Phys.* **340**, 670–687 (2017).
11. C. Poulard, G. Guéna, A. Cazabat, Diffusion-driven evaporation of sessile drops. *J. Phys. Condens. Matter* **17**, S4213 (2005).
12. X. Cai *et al.*, Aggregation-induced emission luminogen-based direct visualization of concentration gradient inside an evaporating binary sessile droplet. *ACS Appl. Mater. Interfaces* **9**, 29157–29166 (2017).
13. Y. Li *et al.*, Gravitational effect in evaporating binary microdroplets. *Phys. Rev. Lett.* **122**, 114501 (2019).
14. H. Hu, R. G. Larson, Evaporation of a sessile droplet on a substrate. *J. Phys. Chem. B* **106**, 1334–1344 (2002).
15. A. Leenaars, J. Huethorst, J. Van Oekel, Marangoni drying: A new extremely clean drying process. *Langmuir* **6**, 1701–1703 (1990).
16. R. K. Arya, Calibration curves to measure concentrations in multicomponent polymeric coatings using confocal Raman spectroscopy. *Int. J. Chem. Eng. Appl.* **2**, 421 (2011).
17. Y. Numata, Y. Iida, H. Tanaka, Quantitative analysis of alcohol–water binary solutions using Raman spectroscopy. *J. Quant. Spectrosc. Radiat. Transf.* **112**, 1043–1049 (2011).
18. Z. Du *et al.*, Investigation of two novel approaches for detection of sulfate ion and methane dissolved in sediment pore water using Raman spectroscopy. *Sensors (Basel)* **15**, 12377–12388 (2015).
19. M. Wagner, Single-cell ecophysiology of microbes as revealed by Raman microspectroscopy or secondary ion mass spectrometry imaging. *Annu. Rev. Microbiol.* **63**, 411–429 (2009).
20. J. P. Hindmarsh *et al.*, Imaging droplet freezing using MRI. *Chem. Eng. Sci.* **59**, 2113–2122 (2004).
21. F. P. Miknis, A. T. Pauli, A. Beemer, B. Wilde, Use of NMR imaging to measure interfacial properties of asphalts. *Fuel* **84**, 1041–1051 (2005).
22. N. C. Reis, R. F. Griffiths, M. D. Mantle, L. F. Gladden, J. M. Santos, MRI investigation of the evaporation of embedded liquid droplets from porous surfaces under different drying regimes. *Int. J. Heat Mass Transf.* **49**, 951–961 (2006).
23. M. D. Mantle, N. C. Reis, R. F. Griffiths, L. F. Gladden, MRI studies of the evaporation of a single liquid droplet from porous surfaces. *Magn. Reson. Imaging* **21**, 293–297 (2003).
24. B. Kresse, M. V. Höfler, A. F. Privalov, M. Vogel, One dimensional magnetic resonance microscopy with micrometer resolution in static field gradients. *J. Magn. Reson.* **307**, 106566 (2019).
25. J. Kind, C. M. Thiele, MRI and localised NMR spectroscopy of sessile droplets on hydrophilic, hydrophobic and superhydrophobic surfaces–Examination of the chemical composition during evaporation. *J. Magn. Reson.* **307**, 106579 (2019).
26. G. Allen, H. J. Bernstein, Intensity in the Raman effect. 3. The effect of deuterium substitution on the intensity of Raman bands of benzene. Can. J. Chem.: *Rev. Can. Chim.* **33**, 1137–1144 (1955).
27. J. Durig, S. Bush, F. Baglin, Infrared and Raman investigation of condensed phases of methylamine and its deuterium derivatives. *J. Chem. Phys.* **49**, 2106–2117 (1968).
28. F. Halverson, The use of deuterium in the analysis of vibrational spectra. *Rev. Mod. Phys.* **19**, 87–131 (1947).
29. M. Ito, M. Suzuki, T. Yokoyama, Raman spectra of hydrogen and deuterium halide crystals. *J. Chem. Phys.* **50**, 2949–2960 (1969).
30. T. R. Stengle, R. C. Taylor, Raman spectra and vibrational assignments for 1,1,1-trihaloethanes and their deuterium derivatives. *J. Mol. Spectrosc.* **34**, 33 (1970).
31. R. Mendelsohn, J. Maisano, Use of deuterated phospholipids in Raman spectroscopic studies of membrane structure. I. Multilayers of dimyristoyl phosphatidylcholine (and its -d54 derivative) with distearoyl phosphatidylcholine. *Biochim. Biophys. Acta* **506**, 192–201 (1978).
32. J. Quinan, S. Wiberley, Infrared and Raman spectra of series of deuterated alcohols. *Anal. Chem.* **26**, 1762–1764 (1954).
33. F. Hidaka, H. Kanno, Raman OD stretching spectral differences between aqueous and alcoholic tetraalkylammonium chloride solutions. *Chem. Phys. Lett.* **379**, 216–222 (2003).
34. C. T. Moonen *et al.*, Comparison of single-shot localization methods (STEAM and PRESS) for in vivo proton NMR spectroscopy. *NMR Biomed.* **2**, 201–208 (1989).
35. U. Klose, Measurement sequences for single voxel proton MR spectroscopy. *Eur. J. Radiol.* **67**, 194–201 (2008).
36. T. M. Mayer, M. P. de Boer, N. D. Shinn, P. J. Clews, T. A. Michalske, Chemical vapor deposition of fluoroalkylsilane monolayer films for adhesion control in microelectromechanical systems. *J. Vac. Sci. Technol. B Microelectron. Nanometer Struct. Process. Meas. Phenom.* **18**, 2433–2440 (2000).
37. M. Hartmann, S. Hardt, Stability of evaporating droplets on chemically patterned surfaces. *Langmuir* **35**, 4868–4875 (2019).
38. J. Frahm, A. Haase, D. Matthaei, Rapid NMR imaging of dynamic processes using the FLASH technique. *Magn. Reson. Med.* **3**, 321–327 (1986).
39. A. Haase, J. Frahm, D. Matthaei, W. Hanicke, K.-D. Merboldt, FLASH imaging. Rapid NMR imaging using low flip-angle pulses. *J. Magn. Reson. (1969)* **67**, 258–266 (1986).
40. J. Hennig, A. Nauerth, H. Friedburg, RARE imaging: A fast imaging method for clinical MR. *Magn. Reson. Med.* **3**, 823–833 (1986).
41. A. K. Bell *et al.*, SFB1194 - A07 - Concentration gradients in evaporating binary droplets probed by spatially resolved Raman and NMR spectroscopy. TUdatalib. https://doi.org/10.48328/tudatalib-824.2. Deposited 22 March 2022.